Structure-property relationship in thioxotriaza-spiro derivative: Crystal structure and molecular docking analysis against SARS-CoV-2 main protease

Mahesha [a], Udaya Kumar A.H. [a], Vindya K.G. [b], Pampa K.J. [c], Rangappa K.S. [b], Lokanath N.K. [a,*]

[a] Department of Studies in Physics, University of Mysore, Manasagangotri, Mysuru, Karnataka 570 006, India
[b] Department of Studies in Chemistry, University of Mysore, Manasagangotri, Mysuru, Karnataka 570 006, India
[c] Department of Biotechnology, University of Mysore, Manasagangotri, Mysuru, Karnataka 570 006, India

ARTICLE INFO

ABSTRACT

Detailed structural and non-covalent interactions in thioxotriaza-spiroderivative (DZ2) are investigated by single crystal structure anslysis and computational approaches. Its results were compared with the previously reported spiroderivative (DZ1). The crystal structure analysis revealed various C–H...O, N–H...O, C–H...N and N–H...S hydrogen bonds involved in constructing several dimeric motifs to stabilize the crystal packing. The differences and similarities in the relative contribution of non-covalent interactions in DZ1 and DZ2 compounds are compared using the Hirshfeld surface analysis and 2D fingerprint plots. The binding energies of specific molecular pairs and homodimers have been obtained using molecule–molecule interaction energy calculation. The hierarchy and topology of pair-wise intermolecular interactions are visualized through energy frameworks. The nature and strength of intra and intermolecular interactions were characterized using non-covalent interaction index analysis and the quantum theory of atoms in molecule approach. Further, molecular docking of compounds (DZ1 and DZ2) with SARS-CoV-2 main protease for COVID-19 is performed. And the superposition of these ligands and inhibitor N3, which is docked into the binding pocket of 7BQY, is presented. The binding affinity of −6.7 kcal/mol is observed, attributed to hydrogen bonding and hydrophobic interactions between the ligand and the amino acid residues of the receptor.

1. Introduction

Spirocyclic derivatives have been widely recognized for their diverse applications ranging from natural products, chiral ligands and organometallic complexes [1–6]. Spiro heterocycles are well-known for their exclusive structural diversity and conformational features that can increase the probabilities of finding bioactive hits and enforce the specificity and potency of ligand-protein binding interactions. Spirocyclane structure comprises two perpendicular rings fused by a single carbon atom to form a rigid tetrahedral center [7]. Fluspirilene, enilospirone, spiraprilat and fenspiride are some examples of important spirane based drugs [8–9]. In recent years, spiroderivatives have been identified as privileged chemotypes for designing and developing an antiviral drug. Spiropyrazolopyridone oxindoles have been investigated as potent inhibitors of dengue

virus NS4B, leading to the design and development of an orally bioavailable preclinical candidate (*R*)-44 with an excellent in vivo efficacy in a dengue viremia mouse model [10–11].

COVID-19 is a life-threatening disease, spreads throughout the world, and there are many ongoing efforts in drug discovery to control the awful impact of the disease on our lives [12–15]. The SARS-CoV-2 main protease plays a significant role in viral replication. Due to its low similarity with human genes is a crucial target for designing and discovering novel COVID-19 drugs. On the other hand, the analysis of binding affinity and structure-property relationship of protein-drug complexes plays an essential role in understanding the molecular mechanism for drug discovery [16–17].

The analysis of nature and its pivotal role in constructing supramolecular frameworks is an emerging area of research in crystallography [18–20]. Supramolecular chemistry is an important tool for tailoring novel esthetic crystal structures with desired physicochemical and biological properties, based on the understanding of chemistry beyond the various bonding and non-bonding interactions [21–25]. The difference in internal structure,

molecular packing, and intermolecular interactions affect the many properties such as filtration, drying, compression, tabletting, flow characteristics, and a drug's dissolution rate.

This article presents the crystal structures of two thioxotriaza-spiroderivatives (DZ1 and DZ2) to address the structural diversity, conformational features, and supramolecular chemistry using combined crystallographic and quantum computational study. To delineate the effect of substituents and to have a qualitative analysis of intermolecular interactions present in the spiroderivatives, we performed Hirshfeld surface analysis, 2D-fingerprint plots and enrichment ratio calculation. The nature and strength of intermolecular interactions between different pairs of molecular fragments in the crystal structure were analyzed and visualized using energy frameworks and Bader's quantum theory of atoms in molecules (QTAIM) analyzes. DFT calculations are performed to understand the stability, physical and chemically active properties of the molecules. Further, the molecular docking study was performed to explore the spiroderivatives' binding affinity with the COVID-19 main protease 7BQY.

2. Experimental and computational section

2.1. Crystal growth

The synthesis and spectroscopic characterizations of the compounds are described in Gopinatha et al. [26]. The supersaturated solution of the compound was prepared using dimethylsulfoxide, dimethylformamide and dimethylacetamide solvents. The solution-filled beakers are partially covered with aluminum foil and kept at room temperature for slow evaporation. Good quality single crystals of the compound for X-ray analysis are obtained from the evaporation of DMSO solvent.

2.2. X-ray diffraction studies

X-ray diffraction intensity data of the compounds were collected on Rigaku XtaLAB mini single crystal X-ray diffractometer at 293 K. The system was operated at (50 kV and 12 mA) 0.6 kW power using graphite-monochromated Mo-Kα radiation ($\lambda = 0.71073$ Å). The quality of the crystal, unit cell dimensions and Bravais lattice type were assessed by indexing the initial reflection frames. An exposure time of 3 s and the scan width of 1° was fixed for the data collection, and the planned data collection strategy was executed using *CrystalClear-SM Expert 2* [27]. The collected data set was processed using d*trek program, and the absorption correction based on multi-scan was also applied. The compounds' crystal structure was solved by direct methods and refined using the full-matrix least-squares against F^2 with an anisotropic thermal motion to describe the thermal parameters of non-hydrogen atoms using *SHELXS* and *SHELXL* programs [28–30]. All the hydrogen atoms attached to the ring carbons were located geometrically. The hydrogen atoms of the substituent groups were positioned from the difference Fourier map and refined with isotropic thermal displacement parameters. The geometrical calculations and crystal packing diagrams were prepared by the crystallographic program *PLATON* and *MERCURY* 4.2.0 software [31–32]. The summary of crystal data and structure refinement parameters are summarized in Table 1.

2.3. Hirshfeld surface and enrichment ratio analysis

Intra and intermolecular contacts of crystal structure in solid-phase are analyzed qualitatively and quantitatively through the molecular Hirshfeld surface using *CrystalExplorer* 17.5 [33]. Hirshfeld surfaces are constructed based on the calculated sum of spher-

Table 1
Crystal data and structure refinement parameters of DZ1 and DZ2.

	DZ1	DZ2
Empirical formula	$C_{20}H_{17}N_3O_3S$	$C_{19}H_{19}N_3O_3S_3$
Formula weight	379.44	433.58
Temperature (K)	293	293
Wavelength (Å)	0.71073	0.71073
Crystal system, space group	Monoclinic, $P2_1/c$	Triclinic, $P\bar{1}$
Unit cell dimensions		
a (Å)	11.1763(8)	9.2990(7)
b (Å)	9.5418(3)	9.6879(7)
c (Å)	17.856(3)	12.954(2)
α (°)	90	69.790(5)
β (°)	97.562(6)	73.587(5)
γ (°)	90	71.030(5)
Volume Å^3	1887.6(5)	1016.4(3)
Z	4	2
Density (calculated) in Mg m^{-3}	1.335	1.417
Absorption coefficient (mm^{-1})	0.197	0.390
F_{000}	792	452
Crystal size (mm)	0.23 × 0.34 × 0.26	0.27 × 0.41 × 0.31
θ range for data collection	3.13° to 27.50°	3.17° to 27.49°
Index ranges	$-14 \leq h \leq 12$	$-11 \leq h \leq 12$
	$-12 \leq k \leq 11$	$-12 \leq k \leq 12$
	$-20 \leq l \leq 23$	$-16 \leq l \leq 12$
Reflections collected	8075	5881
Independent reflections	4266	4520
	[$R_{int} = 0.0799$]	[$R_{int} = 0.0252$]
Refinement method	Full matrix	Full matrix
	least-squares on F^2	least-squares on F^2
Data/restraints/parameters	4266/0/246	4520/0/255
Goodness-of-fit on F^2	1.065	1.054
Final [$I > 2\sigma(I)$]	$R1 = 0.0680$	$R1 = 0.0798$
	$wR2 = 0.1597$	$wR2 = 0.2166$
R indices (all data)	$R1 = 0.1086$	$R1 = 0.1074$
	$wR2 = 0.1857$	$wR2 = 0.2343$
Largest diff. peak and hole	0.487 and −0.389 e Å^{-3}	0.965 and −0.837 e Å^{-3}
CCDC No.	1,888,913 (reported)	1,959,033

ical atom electron densities of the promolecule and procrystal. The molecular Hirshfeld surface is the frontier region where the electron density distribution is dominated by the contribution of the molecule internal to the surface and of the neighbouring molecules external to the surface [34]. The normalized d_{norm} surface helps identify the intermolecular interaction regions in the crystal structure based on the atom's vdW radii, distance from the surface to the nearest nucleus inside (d_i) and outside the surface (d_e). The decomposition of the contact surface by a particular elemental pair and the percentage contribution of those pairs to the surface is vital to analyze the molecular interactions from the fingerprint plots (FP) [35]. The percentage contribution of the pair of elements (actual contacts) obtained in the Hirshfeld surface is used to calculate the enrichment ratio (ER). It is the ratio between the proportion of actual contacts and the random contacts (calculated). ER is larger than unity for pairs of elements with a higher propensity to form contacts, while pairs that tend to avoid contacts yield an ER value lower than unity [36].

2.4. Interaction energy and energy frameworks

To quantify and visualize the topology of the packing of molecules in crystal by overall interactions, energy framework analysis has been performed using *CrystalExplorer* 17.5. The molecular interaction energies were estimated from a single-point molecular wavefunction at CE-B3LYP/6–31G(d,p) using the crystallographic information file (cif) of the compound. The interaction energy calculation was executed for the cluster of molecular fragments generated (3.8 Å) around the central molecule by crystallographic symmetry operation (Symop). The color-coded mapping for the individual molecules helps to identify the pair-wise interaction energies with the central molecule. The electrostatic (E_{ele}), polarization (E_{pol}), dispersion (E_{dis}) and repulsion (E_{rep}) energy within the crystal has been estimated by adding scaling factors of the corresponding energy model. The energy frameworks are the 3-D topology of interactions constructed using the various energy components (E_{ele}, E_{dis} and E_{tot}) obtained from the interaction energy calculations [37–38].

2.5. Density functional theory calculations

The ground state electronic structure of the compounds was optimized without any symmetry constraints using the DFT method with B3LYP exchange-correlation functional at 6-311+G(d,p) basis set. The geometry of the examined systems was optimized in the gas phase. Vibrational frequency calculations were performed to confirm the correspondence of optimized geometries to local minima on potential energy surface. All the calculations were performed using the *Gaussian*16 [39], and visualized *GaussView*6 [40] software was used to generate the molecular orbitals (MOs) and molecular electrostatic potential figures.

2.6. Analysis of topological parameters (QTAIM calculations)

Bader's QTAIM analysis is a powerful tool for understanding the molecule's covalent, ionic and hydrogen-bonding interactions based on the electron density distribution. The nature and strength of interactions in the molecule are assessed using the values of electron density and its Laplacian, potential, kinetic energy density, and total energy densities at the bond critical points (BCPs). The interaction energies of the intra and intermolecular interactions were also estimated through the $E_{int} = -0.5V(r) \times 2625.5$ (kcal/mol) [41]. Negative region of sign(λ_2)ρ with larger value are indicative of attractive interactions, while if the sign(λ_2)ρ is positive indicates the steric interaction. The green-colored spikes near

zero indicate the weak van der Waals interactions. The 2-D scatter plots are generated to understand the strength and nature of non-covalent interaction with the spikes associated with the respective interaction. All the above analyzes were carried out using the *Multiwfn* 3.7 [42] and visualized by *VMD* software [43] based on Gaussian cube files generated by *Multiwfn*.

2.7. Molecular docking

Molecular docking is a structure-based drug design approach to identify and explore the essential amino acid interactions between the biomolecule and ligands with low energy conformation. *In silico* molecular docking studies were carried out to explore the binding modes and affinities of novel thioxotriaza-spiroderivatives, DZ1 and DZ2, against the main protease of SARS COVID-19 (Mpro) using MGL tools 1.5.6 with *AutoDock Vina* [44]. The binding sites were defined using the grid box with an energy range of 4 and exhaustiveness of 8. Kollman charges define each amino acid's value derived from the corresponding electrostatic potential, and the polar hydrogen atoms were added to the protein. The total Kollman charge added for the protein in this study was four, while the ligand is zero. The default settings in Autodock Vina employed the energy minimization of the protein and ligand preparation. The main protease of COVID-19 (PDB ID:7BQY) was downloaded from the protein data bank, and the coordinates of the DZ1 and DZ2 were taken from the X-ray analysis (in CIF format) saved in PDB format for docking input. *Biovia Discovery Studio* 2019 Client [45] molecular visualizer was used to presenting the output files and measure distances, angles, and torsion angles among atoms of interest. The key residues that form the substrate-binding pocket of 7BQY were identified from the protease's binding mode with N3 by Jin et al. [46]. Further, a 2D diagram of the receptor-ligand interactions in the complex is generated to represent the nature of the active interactions.

3. Results and discussion

3.1. Single crystal X-ray diffraction analysis

The single crystal X-ray diffraction studies reveal that the compound 1 (DZ1) and 2 (DZ2) are crystallized in the monoclinic space group $P2_1/c$ and triclinic space group $P\bar{1}$ respectively. The asymmetric unit of DZ1 contains a unique molecule with $Z = 4$, whereas DZ2 crystallizes along with a lattice solvent (DMSO). ORTEP diagrams of the DZ1 and DZ2 with the thermal ellipsoids drawn at 50% probability are presented in Fig. S1 (S;supplementary information) and Fig. 1 [26]. The bond lengths, bond angles and torsion angles of both the structures are tabulated (Tables S1–S3) and compared with the optimized electronic structures. Puckering analysis disclosed that the cyclic 5-membered Cg(1) ring comprised of the atoms C7/C8/C9/C10/N1, is puckered with the puckering amplitude Q(2) = 0.259(3) Å and 0.244(5) Å. The angle for the ring conformation on the puckering surface [$\phi(2)$] is 294.3(6) and 114.2(11) for DZ1 and DZ2, respectively, resulting in an envelope conformation on the C9 [47]. The envelope configuration of this ring is further substantiated from the pseudorotation parameter P = 97.4(4) and 277.1(7), $\tau(M)$ = 25.8(1) and 24.2(3) for the reference bond N1−C7. The fused 6-membered Cg(2) ring in DZ1 (C10/C16/C17/N1/C13) is in E form with puckering amplitude (Q) = 0.168(3) Å, θ = 122.6(10)°, Phi = 60.8(11)°, whereas in the DZ2 it is in a twist conformation with puckering parameters, $q2$ = 0.244(4)Å, $\varphi(2)$ = 293.2(10)°. The fused Cg(1) and Cg(2) rings constitute the thioxotriaza-spiromoiety, and they are nearly perpendicular to each other, as evident from the dihedral angle of 83.55° and 85.43° in DZ1 and DZ2. The Cg(1) ring makes a dihedral angle of 13.26° (DZ1) and 10.92° (DZ2) with respect
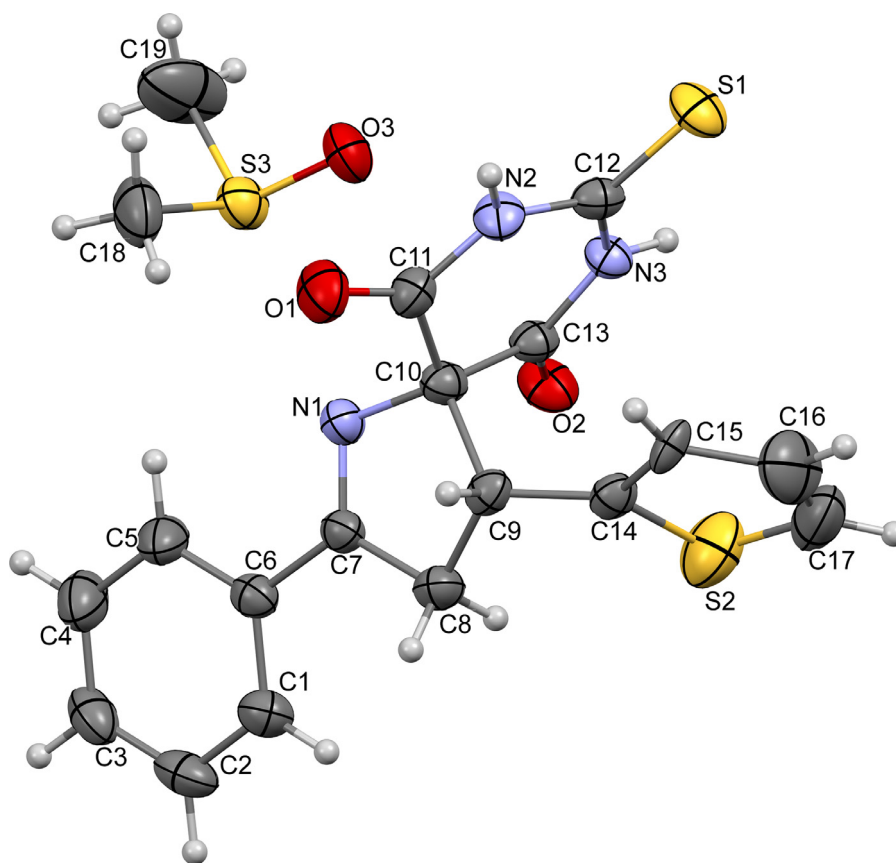
Fig. 1. ORTEP diagram of DZ2 compound with thermal ellipsoids are drawn at 50% probability level.

to the mean plane of the attached phenyl ring. The dihedral angle of 64.73° is observed between Cg(1) and methoxy substituted phenyl ring in DZ1. Thiophene ring in DZ2 makes a dihedral angle of 66.23° with the Cg(1) ring of thioxotriaza-spiromoiety. The phenyl ring exhibits − and + antiperiplanar conformation [C1-C6-C7-N1 = −169.30° (DZ1) and 171.90° (DZ2)] with respect to thioxotriaza-spiromoiety. The methoxy substituted phenyl ring in DZ1 exhibits anti-clinal [C10-C9-C14-C15 = −92.96°] whereas the replaced thionyl ring in DZ2 exhibits a (-) syn-clinal conformation [C10-C9-C14-S2 = −87.17° (19)].

The crystal structure of the compounds DZ1 and DZ2 are stabilized by various intra and intermolecular hydrogen bonding and π-π stacking interactions (Table S4). In DZ1, C5-H5...N1 and di-hydrogen (H...H) intramolecular interactions form S(5) and S(6) loops, whereas in DZ2, C8-H8A...S2 and C5-H5...N1 interactions forms supramolecular rings with graph-set notation S(5) (Fig. S2). In DZ1, the central symmetry independent molecule forms four inversion-related dimers, two with ring motif of $R_2^2(8)$ by N2-H2...O1 and N3-H3...S1 hydrogen bonds and other two, $R_2^2(12)$ and $R_2^2(16)$ loop formed through C8-H8A...O1 and C18-H18...O2 inter-contacts. The $R_2^2(8)$ dimers propagate alternatively along the *a*-axis to generate the one-dimensional zig-zag chain. The $R_2^2(12)$ loop interconnects the 1-D chain, leading to forming a 2-D planar sheet in the *ab* plane (Fig. S3a). Further, C18-H18...O2 and C20-H20B...S1 (symmetry: 1-*x*, −1/2+*y*, 1/2-*z*, D(I–J) = 2.90 Å, X–I...J = 160°, where I and J are planes and X; C20) short contacts also significantly contribute to the packing of molecules to produce 3-D supramolecular architecture of the DZ1 (Fig. S3b). In DZ2, the presence of lattice solvent DMSO participated in the various intermolecular interactions to stabilize the crystal packing (Fig. S4). The strong N2-H2...S1 interaction between the inversion related molecules results in $R_2^2(8)$

supramolecular synthon (Fig. 2b) interconnected by C17−H17...O1 hydrogen bond to form meshed architecture. The lattice solvents which are related by an inversion are also forms $R_2^2(8)$ loop *via* C18-H18A...O3 interactions (Fig. 2c). The dimeric solvents with $R_2^2(8)$ are trapped at the center of four DZ2 molecules by C16-H16...S3, N3-H3...S3 and N3-H3-O3 intermolecular interactions. Further, C3-H3A...O2 (symmetry:−*x*, 2−*y*, −1−*z*, D(I–J) = 2.628 Å, C3-I...*J* = 123°) and C2-H2A...S1 (symmetry:*x*,1+*y*, −1+*z*, D(I-J) = 2.932 Å, C2-I...*J* = 151°) also contribute to the overall crystal packing stabilization. The supramolecular architecture of DZ2 shows the trapping of solvent molecules in the alternative rhombus-shaped synthons along the *c*-axis (Fig. 2).

3.2. Hirshfeld surface and enrichment ratio analysis

The molecular Hirshfeld surfaces of DZ1 and DZ2 compounds have been mapped over d_{norm} and shape-index properties. The Hirshfeld surface analysis well reproduced the results of the supramolecular architecture of crystal structure and enlightened intermolecular interactions quantitatively. The d_{norm} mapped surface was mapped with a color scale between −0.3 (blue) and +1.0 a.u (red). The two-dimensional (2D) FPs were displayed using the expanded 0.6−2.4 Å view on the graph axes. The information is present in Table S4 is summarized effectively by the bright and faint red spots on the Hirshfeld surface [48,49].

The intense red spots in region 1 involving the interaction between two inversion-related thioxotriaza-spiromoieties resulting in complementary N-H...O interaction. A similar bright spot on N3-H3 and S1 in region 2 results from the $R_2^2(8)$ inversion dimer *via* N-H...S interaction. Two different faint red spots 3 and 4 near the meta positioned oxygen (O1 and O2) indicates the C8-H8A...O1 and C18-H18...O2 interaction, which leads to the con-
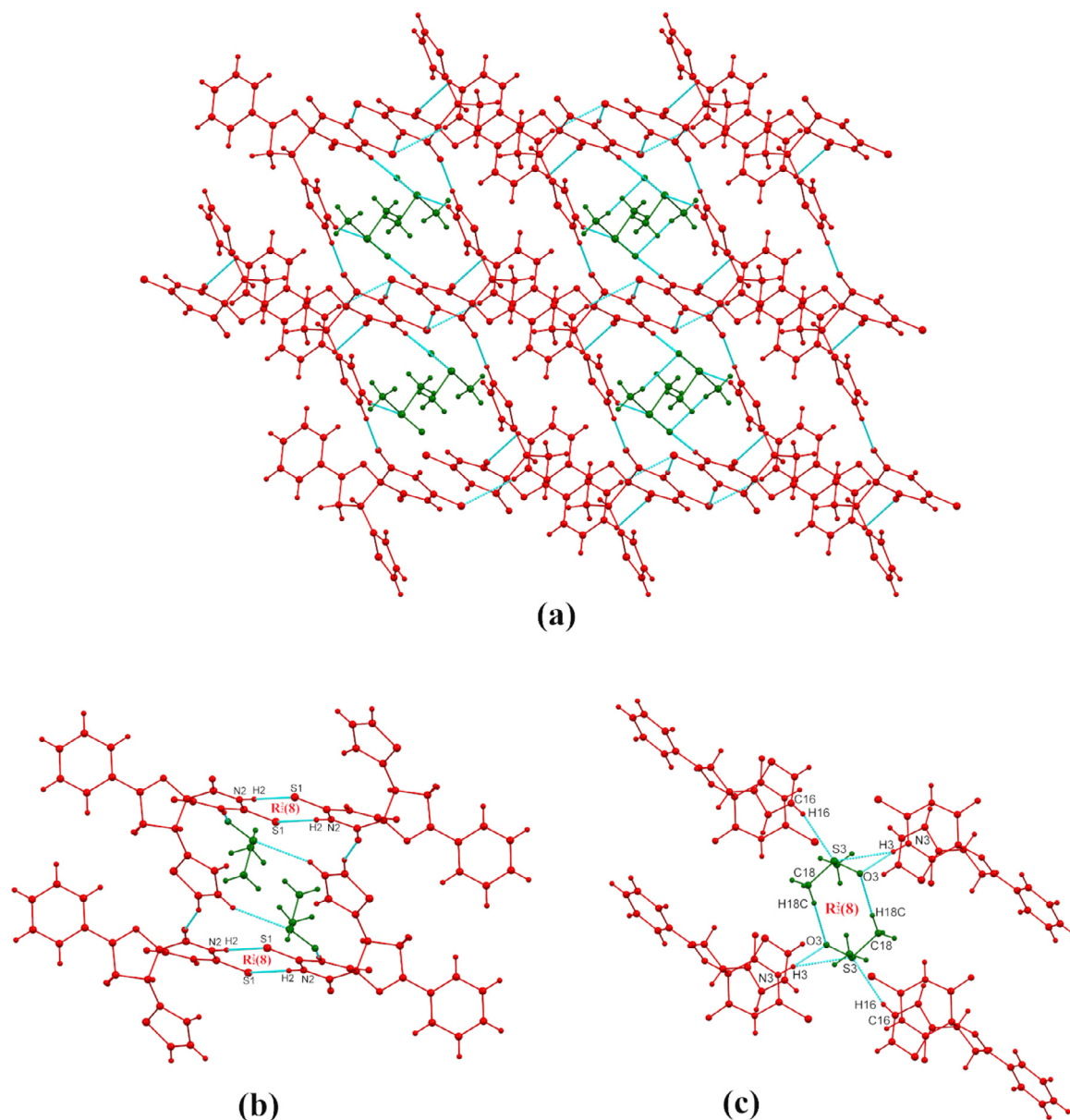
Fig. 2. (a) 3-D packing of molecules and (b) hydrogen bonding interactions between guest solvent and DZ2 molecule.

struction of $R_2^2(12)$ and $R_2^2(16)$ inversion dimers, respectively. Further, the light red spots in the region 5 and 6 support the presence of C16–H16...N1 and C20–H20B...S1 interaction in the crystal packing analysis (Fig. 3a,b).

Another essential feature of the supramolecular frameworks is the effect of the solvate molecules. In DZ2, the lattice DMSO molecule is involved in various non-covalent interactions, significantly contributing to the supramolecular architecture. Both -O and -S group of the DMSO acts as acceptors for the same donor (-NH) of spiromoiety to form N3-H3...O3/S3 contacts indicated by bright red spot 1. Two dark red spots 2 near the thioxotriaza-spiroring indicates the N-H...S interaction between inversion related $[R_2^2(8)]$ dimeric molecules. A similar bright spot near 3 indicates the interaction between meta positioned –O with –CH group of thiophene (C17–H17...O1). The light red spots 4, 5 and 6 indicates a weaker C18–H18C...O3, C16–H16...S3 and C2–H2A...S1 contacts in the self-assembly of DZ2 (Fig. 3c,d).

FPs are extremely sensitive to the chemical environment and are unique to a particular molecule. Fig. S5 shows the fingerprint plots and the percentage contributions of the major non-covalent

interactions to the molecular Hirshfeld surface. The dihydrogen (H...H) contacts are the shortest contacts depicted as the sharp spike at the center ($d_e = d_i \approx 1.1$ Å). They contribute significantly to the total Hirshfeld surface with 35 and 39.7% in DZ1 and DZ2, respectively. Besides, the C...H intermolecular interactions involved in the C...H–C (π) contacts ($d_e + d_i \approx 3.4$ Å) with the contribution of 23.6 and 16.4%. The two symmetrical spikes at the vicinity of $d_e + d_i \approx 2.2$ Å resembles the H...O/O...H interactions with the contribution of 17.7 and 19.2%, respectively. Regarding the H...S contacts, the symmetrical spikes observed at $d_e + d_i \approx 3.0$ Å for DZ1 with 15.3%, whereas in DZ2, the spike appears near $d_e + d_i \approx 3.2$ Å with 18.5%. The relatively greater contribution of H...S and H...O interactions in DZ2 is observed due to the effect of lattice solvent molecule (DMSO) and the replacement of phenyl by thiophene ring.

We have also determined the enrichment ratios (ER) of the intermolecular contacts for DZ1 and DZ2 compounds to reveal the propensity of two chemical species to be in contact [50]. Tables 2a and 2b presents the E_{XY} values for the two molecules derived from the Hirshfeld surface analysis results. The largest proportion (S_H) of
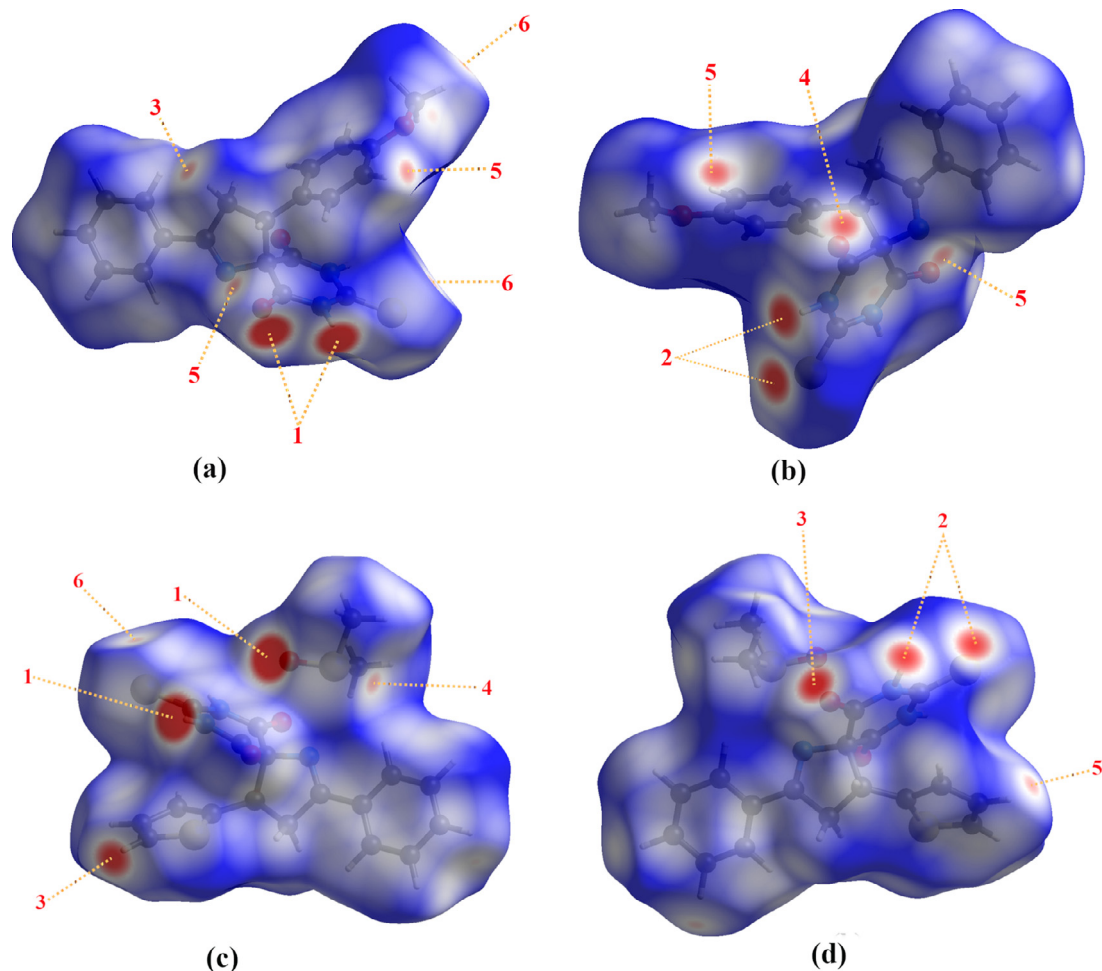
Fig. 3. Hirshfeld surface for the compound DZ1 and DZ2 presented in two different orientations.

Table 2a
The enrichment ratios (ER) for the DZ1 compounds. Values in italics at the top of the table are the data obtained from CrystalExplorer. The (ER) were not considered when the random contacts were lower than 0.9%.

	H	O	N	C	S
H	*35*		Actual contacts		
O	*17.7*	*1.1*			
N	*5*	*0.8*			
C	*23.6*	*1*		*0.1*	
S	*15.3*	*0.1*		*0.1*	
Sx	65.8	10.9	2.9	12.4	7.75
H	43.30		Random contacts		
O	14.34	1.19			
N	3.82				
C	16.32	2.70		1.54	
S	10.20	1.69		1.92	
H	0.81		Enrichment ratio		
O	1.23	0.93			
N	1.31				
C	1.45	0.37			
S	1.50	0.06			

Table 2b
The enrichment ratios (ER) for the DZ2 compound.

	H	O	N	C	S
H	*39.7*		Actual contacts		
O	*19.2*	*0.3*			
N	*1.4*	*0.2*			
C	*16.4*	*0.9*		*1.7*	
S	*18.5*	*0.5*		*0.1*	1.1
Sx	67.45	10.7	0.8	10.4	10.6
H	45.50		Random contacts		
O	14.43	1.14			
N	1.08	0.17	0.01		
C	14.03	2.23	0.17	1.08	
S	14.30	2.27	0.17	2.20	0.01
H	0.87		Enrichment ratio		
O	1.33	0.26			
N	1.30				
C	1.17	0.40		1.57	
S	1.29	0.22			

hydrogen atoms (65.8 and 67.45 %) at the molecular surfaces indicates the significant contribution of dispersive forces to the crystal packing. According to the above, the EHH values (0.81 and 0.87) of less than unity are observed for H…H contacts. The E_{HS} and E_{OH} values are significantly higher than unity for both the compounds, showing a high propensity to form C–H…S/O and N–H…S/O hydrogen bonds. The likelihood to form π…π stacking interactions

are more in DZ2, which is reflected by the increased E_{CC} value of 1.55, which are associated to C…C (π-π) interaction according to the literature. This leads to the relatively low tendency to C…H contacts in DZ2 with E_{CH} of 1.17, compared to DZ1 (E_{CH} = 1.45).

3.3. Interaction energy and energy frameworks

The interaction energy calculation was performed to analyze the molecule–molecule interactions of a specific molecular groups
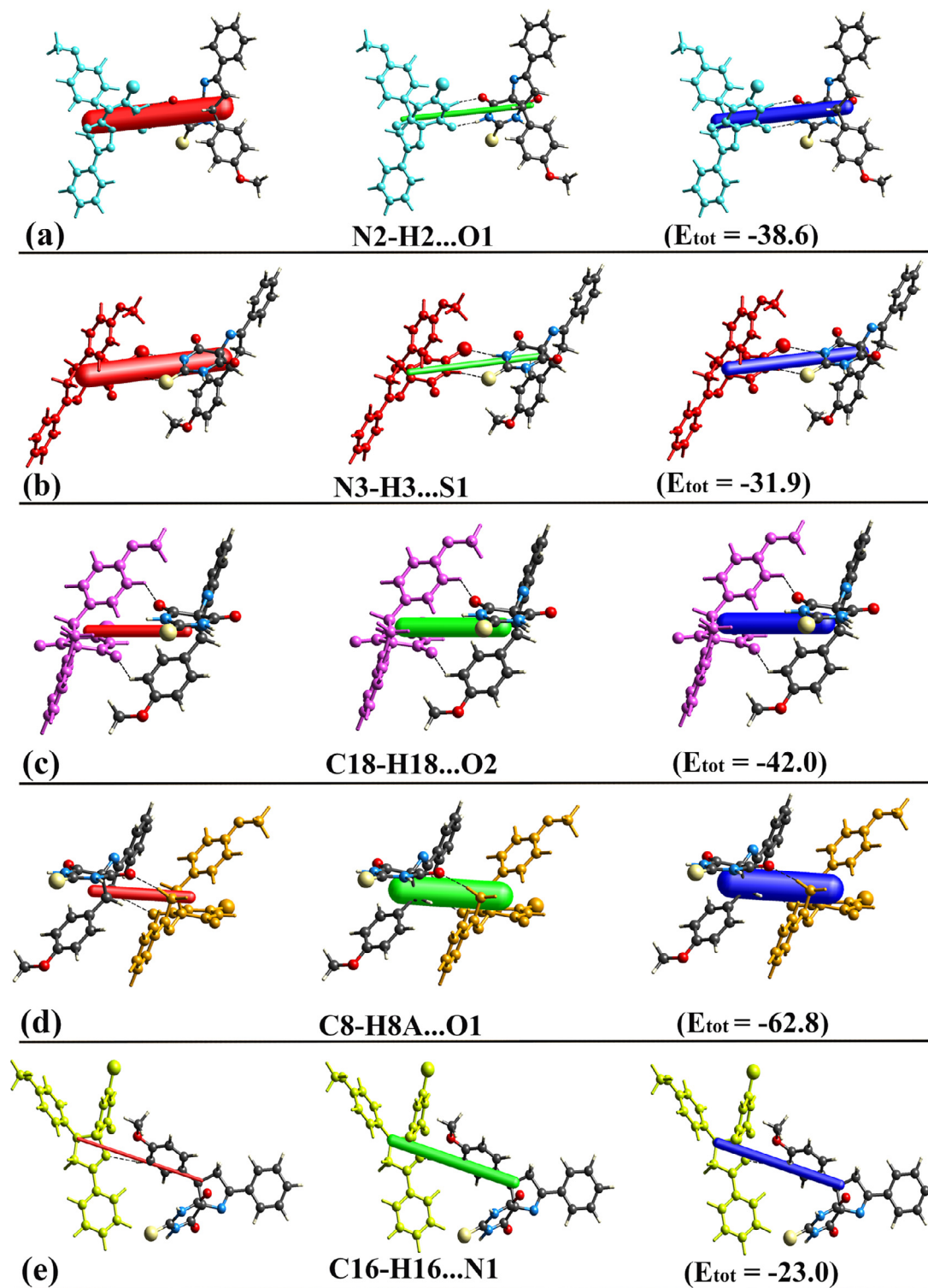
(a)   N2-H2...O1   (E_{tot} = -38.6)

(b)   N3-H3...S1   (E_{tot} = -31.9)

(c)   C18-H18...O2   (E_{tot} = -42.0)

(d)   C8-H8A...O1   (E_{tot} = -62.8)

(e)   C16-H16...N1   (E_{tot} = -23.0)

Fig. 4. The interaction energies of hydrogen bond and molecular dimers of DZ1 compound in kJ·mol^{-1}.

and not only as specific atom-atom contacts with any directional specificity [51–53]. By the topology analysis of the pair-wise molecular interactions (Table S5), it can be readily seen how they energetically participate in forming the 3-D supramolecular architecture.

In the DZ1 compound, the cyclic pair of molecules involving two C–H...O contacts (Fig. 4c,d) are the most relevant interactions with the larger contribution of dispersion component (E_{dis} = −68

and −43.8 kJ/mol). Another stronger interaction by N–H...O and N–H...S contacts responsible for forming the hydrogen-bonded dimers also contributes to the total energy with a significant electrostatic component (E_{col} = −58 and −51.9 kJ/mol). The repulsion energy associated with the close N...O and N...S contacts is also large. However, the electrostatic and dispersion energy components make this interaction the strongest in the crystal (Fig. 4a,b). Further, in contrast to the C–H...N interaction that connects the
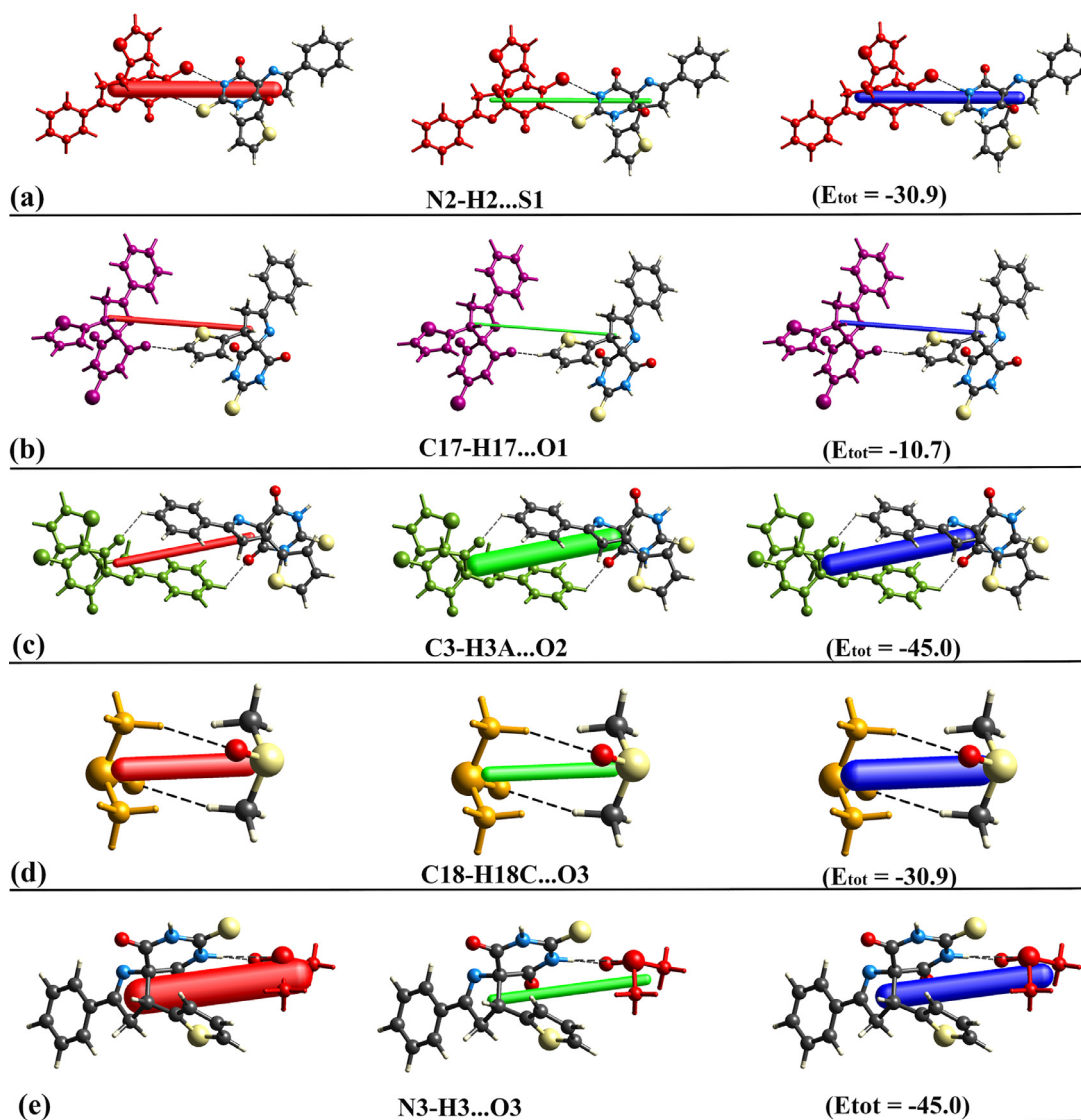
Fig. 5. The interaction energies of hydrogen bond and molecular dimers of DZ2 in kJ·mol^{-1}.

adjacent 1–D chains is moderately strong with $E_{dis} = -31.3$ kJ mol^{-1} (Fig. 4e).

The N–H⋯S and C–H⋯O hydrogen bonds with the supramolecular homosynthon between the inversion-related molecule are the most significant interaction in DZ2 (Fig. 5a–c). The cyclic pair of molecules involving two N–H⋯S hydrogen bonds is evident from the strong electrostatic interactions ($E_{ele} = -39.2$ kJ/mol), whereas C–H⋯O interaction involves a dominant dispersion component ($E_{dis} = -53.7$) to contribute to the total energy. The presence of the highly polarized sulfur group in thioxotriaza-spiromoiety adds to the electrostatic component of the interaction energy. Even the C–H⋯O hydrogen bonds are weak in nature, they can act together cooperatively to offer stable structural motifs. The lattice solvent DMSO acts as a strong acceptor for the host molecule, leading to the formation of N–H⋯O and N–H⋯S contacts with the predominant electrostatic component (Fig. 5e). The C18–H18C⋯O3 hydrogen-bonded dimer in guest–guest interaction is similar to the secondary synthon that connects the 1-D linear chain with significant electrostatic and dispersion energies (Fig. 5d).

The role of predominant intermolecular interactions in the context of the overall packing of molecules in the crystalline phase was analyzed by calculating the pair-wise interaction energies involved in the first coordination sphere (3.8 Å). The interaction energies such as, electrostatic ($E_{ele} = -191.95$ kJ/mol), polarization ($E_{pol} = -30.34$ kJ/mol), dispersion ($E_{dis} = -206.07$ kJ/mol), repulsion ($E_{rep} = 169.45$ kJ/mol) and total interaction energy ($E_{tot} = -258.91$ kJ/mol) values are obtained for the cluster of fragments of DZ1. The interaction energies, $E_{ele} = -75.24$ kJ/mol, $E_{pol} = -20.8$ kJ/mol, $E_{dis} = -110.5$ kJ/mol, $E_{rep} = 126.2$ kJ/mol and $E_{tot} = -113.4$ kJ/mol are the obtained values for the cluster of fragments of DZ2. Energy frameworks for DZ1 and DZ2 compounds (Figs. S6 and S7) immediately show that the total interaction energies for molecular pairs largely contribute by the dispersion component. The energy framework closely mirrors the more anisotropic topological environment for DZ2 compared to DZ1.

3.4. Analysis of topological parameters (QTAIM calculations)

In QTAIM molecular graph, the particular regions with significant non-covalent interactions in the molecule can be identified to analyze their nature and strength based on their topology of the electron density distribution [54]. A reduced density gradient-based NCI indexed model for the compounds DZ1 and DZ2 in 3D space is displayed in Fig. 6 with an isosurface value of 0.06. The molecules show distinct weak intramolecular hydrogen bonding, and van der walls interactions are identified (Table 3).
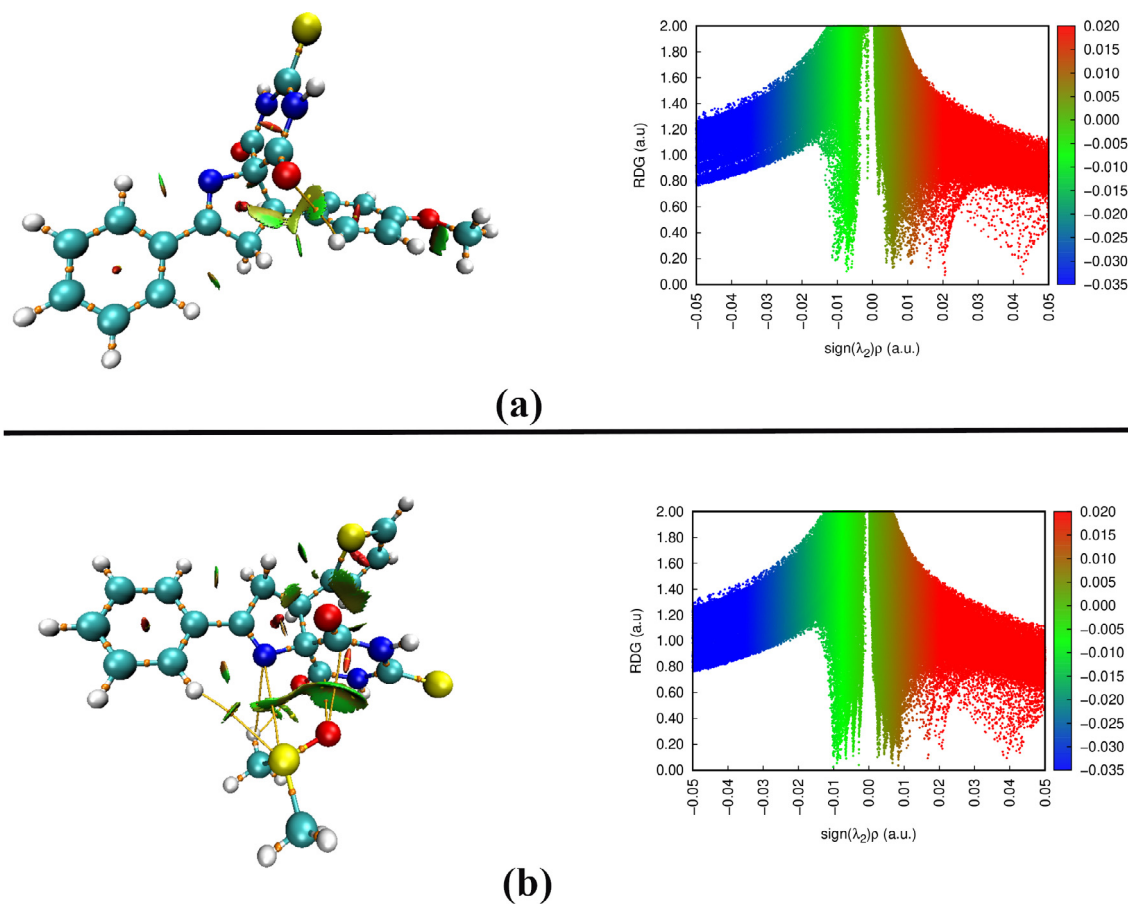
Fig. 6. 3D NCI plots with an isosurface value of 0.6 and plots of RDG against electron density multiplied by the sign of the second Hessian eigenvalue [sign(λ2)ρ(r)] for DZ1 (a) and DZ2 (b) compounds.

Table 3
The electron density [$\rho(r)$] and its Laplacian [$\nabla^2\rho(r)$], kinetic energy density [G(r)], potential energy density [V(r)], energy density [H(r)] and interaction energy (E_{int}) for non-covalent interactions.

Compound	Bondinginteraction	$\rho(r)$(a.u.)	$\nabla^2\rho(r)$(a.u.)	G(r)(a.u.)	V (r)(a.u.)	H(r)(a.u.)	E_{int}(kcal/mol)
DZ1	N2-H2...O1	0.0272	0.0995	0.0228	−0.0208	0.0020	27.30
	N3-H3...S1	0.0189	0.0409	0.0104	−0.0107	0.0002	14.04
	C18-H18...O2	0.0072	0.0297	0.0061	−0.0048	0.0013	6.30
	C19-H19...O2	0.0063	0.0266	0.0053	−0.0041	0.0012	5.38
	C8-H8A...O1	0.0086	0.0296	0.0064	−0.0055	0.0009	7.22
DZ2	N3-H3...S1	0.0195	0.0417	0.0107	−0.0110	0.0003	14.44
	C18-H18...O3	0.0114	0.0358	0.0078	−0.0067	0.0011	8.79
	C19-H19...O3	0.0106	0.0336	0.0073	−0.0062	0.0010	8.13
	C3-H3...O2	0.0061	0.0232	0.0048	−0.0037	0.0010	4.85

In DZ1, red-colored disks are observed in the middle of all four rings to indicate the ring strain, and the steric repulsion is majorly observed in the thioxotriaza-spiroring. The presence of C–H...O intramolecular interaction is validated by green isosurface between O2 and methoxy substituted phenyl –CH (H19) and C–H...N contacts from N1 and phenyl –CH (H5) is identified as small green disks. The weak dispersive nature of various dihydrogen (H1...H8A, H19...H8B and H18...H20A) bonds which are participated in the formation of S(6) rings are also elucidated *via* NCI isosurface (Fig. 6a). Similarly, weak C–H...O, N–H...O and di–hydrogen intramolecular interactions of DZ2 are indicated by green disk and diffused surface. In DZ2, the molecule and the solvent DMSO are connected by C18–H18A...N1, C18–H18A...O1 hydrogen bonds and lone pair-π interactions between O3 of DMSO and π electron system of Cg(2) ring (Fig. 6b). The red disks in the middle of the rings indicate the effect of ring strain for the molecular interac-

tions, and the major steric repulsion is observed at the ring center of the thiophene moiety. The 2-D scatter plot for the compounds DZ1 and DZ2, evident the weak van der Walls interactions by the spikes in the range 0 to −0.01 (green) and steric repulsion by red spike near +0.02 and +0.04.

3.5. Density functional theory studies

The geometry optimization was conducted using initial atomic coordinates derived from the X-ray crystal structures of DZ1 and DZ2. The overlay of optimized electronic structures shows the best conformational fit with the experimental crystal structures (Fig. S8). It is confirmed by the root mean square deviation (rmsd) of 0.201 and 0.126 for DZ1 and DZ2. The comparison of theoretically calculated and experimentally determined geometrical parameters (bond lengths, bond angles, and torsion angles) with the corre-
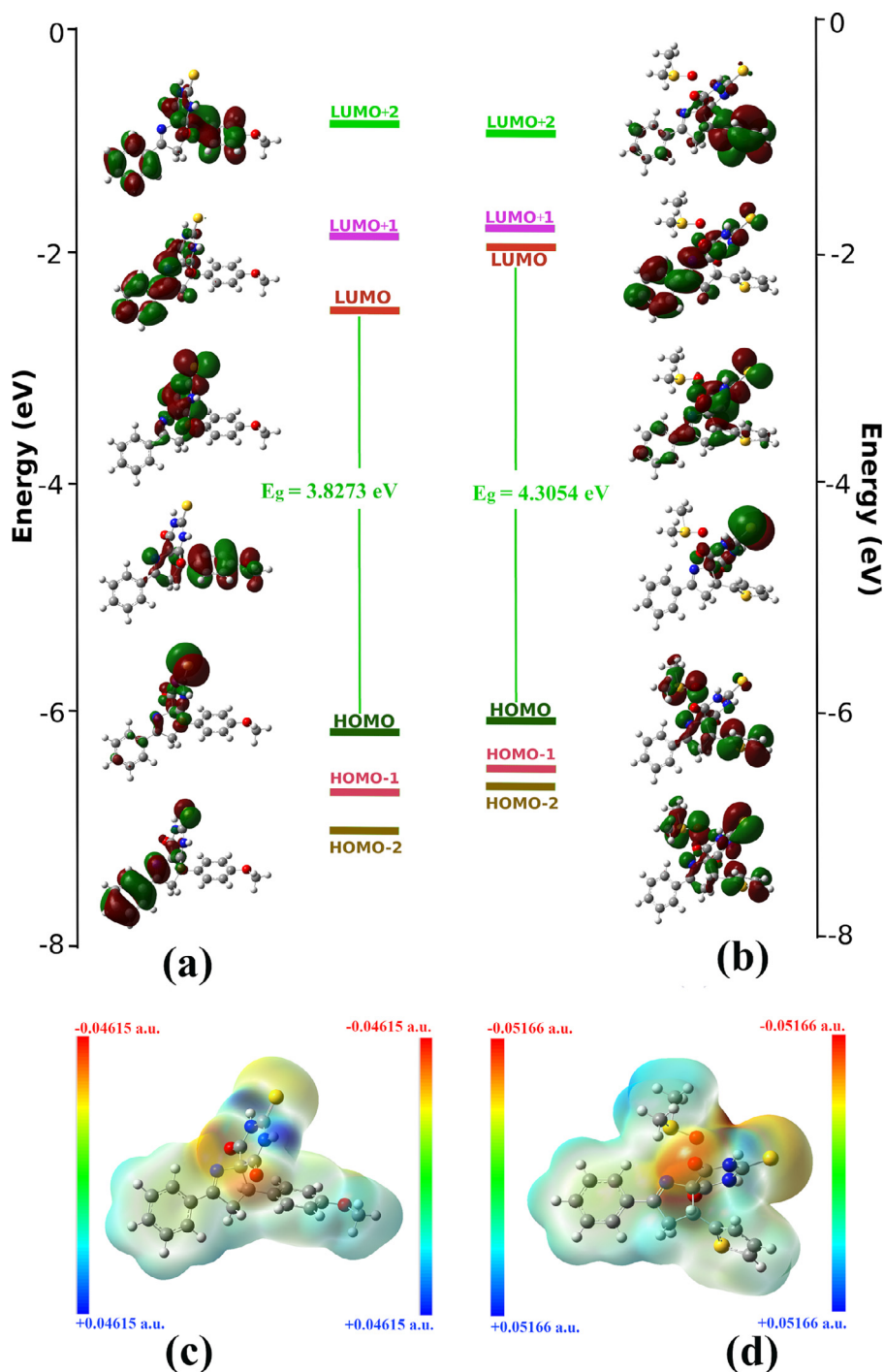
Fig. 7. Frontier Kohn–Sham molecular orbitals of DZ1 (a) and DZ2 (b) compounds with energy level diagram. Molecular electrostatic potential map of DZ1 (c) and DZ2 (d) compounds.

sponding correlation coefficients are given in supplementary Tables S1–S3. The ground state optimization energy of 1054.5 and 1500 Hartree is observed for DZ1 and DZ2, respectively. The 3D plots of the frontier molecular orbitals and their energy profile reveal the spatial distribution of the electron system in the DZ1 and DZ2 molecules. Selected molecular orbitals for compounds are shown in Fig. 7a,b, from LUMO+2 to HOMO-2 principally. It can be seen from the MO's diagrams that the HOMO is majorly located around methoxy substituted phenyl ring, and LUMO is distributed over the thioxotriaza-spiroring moiety in DZ1. In DZ2, the HOMO is located on Cg(2) ring of spiromoiety, whereas LUMO is distributed among all the molecule rings. The energies of HOMO

level are −6.3403 and −6.2793 eV, whereas the LUMO energies are −2.5130 and −1.9739 eV for DZ1 and DZ2, respectively. Negative values for E_{HOMO} and E_{LUMO} energy levels imply the relative stability of both the compounds. HOMO-LUMO energy gaps of DZ1 and DZ2 are respectively 3.8273 and 4.3054 eV. In DZ2, the HOMO-1 and HOMO-2 FMOs are close to HOMO orbital energy due to the effect of lattice solvent. The compounds' global and local reactive parameters are derived from the HOMO-LUMO energy gap values (Table 4). A total electron density distribution-based molecular electrostatic potential (MEP) map was generated for both the compounds to unveil the reactive sites by analyzing the low and high electrostatic potential region (Fig. 7c,d). Both negatively and

Table 4

The energy values and global reactive descriptors of DZ1 and DZ2 compounds.

Parameter	DZ1	DZ2
E_{HOMO}	−6.3403	−6.2793
E_{LUMO}	−2.5130	−1.9739
Energy gap (eV)	3.8273	4.3054
Ionization energy (eV)	6.3403	6.2793
Electron Affinity (eV)	2.5130	1.9739
Electronegativity (eV)	4.4266	4.1266
Chemical Potential (eV)	−4.4266	−4.1266
Global hardness (eV)	1.9136	2.1527
Global softness (eV^{-1})	0.5226	0.4645
Electrophilicity index (eV)	5.1198	3.9553

positively active regions of DZ1 and DZ2 are significantly associated with the thioxotriaza-spiromoiety. The high electrostatic potential is distributed around the sulfur group and oxygen (O1 and O2) in ring 3 suitable for an electrophilic attack, whereas the nucleophilic active sites are observed in the vicinity of nitrogen (N2 and N3) atoms. This implies that the most susceptible sites on the studied compounds for favourable interactions with an electron-rich species are located on the thioxotriaza-spirounit.

3.6. Molecular docking

The molecular docking studies revealed how heterocyclic spirobased ligands might bind to the SARS COVID-19 main protease (7BQY). The docked molecules are fitted to interact with the active site of 7BQY protease. Binding affinity is a key index to understand the strength of the interaction between the ligand (inhibitor) and biomolecule. It is majorly affected by strong hydrogen bonding, electrostatic interactions and, hydrophobic and van der Waals forces [55]. The non-covalent interactions involved in constructing the supramolecular solid architecture of DZ1 and
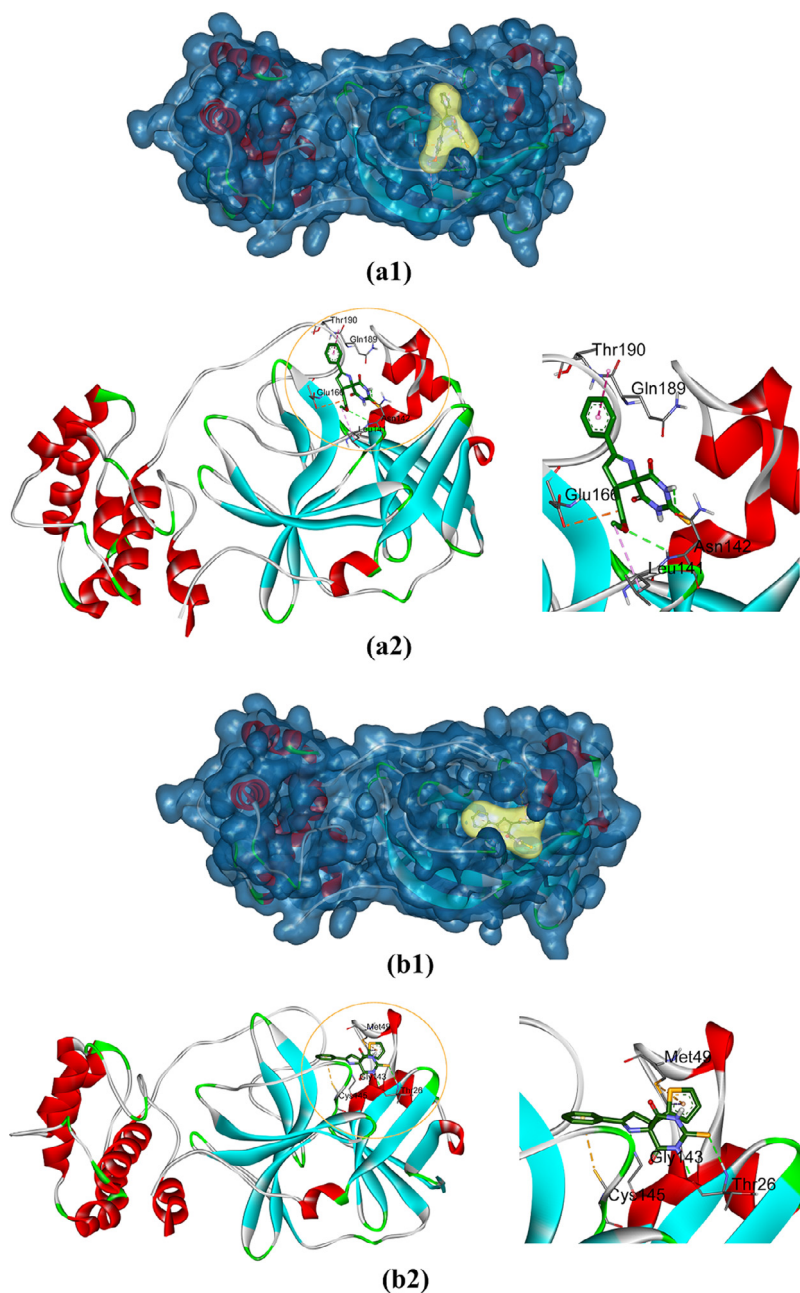

Fig. 8. Docking poses and orientation of DZ1 (a1 and a2) and DZ2 (b1 and b2) in the active sites of COVID-19 protein 7BQY.
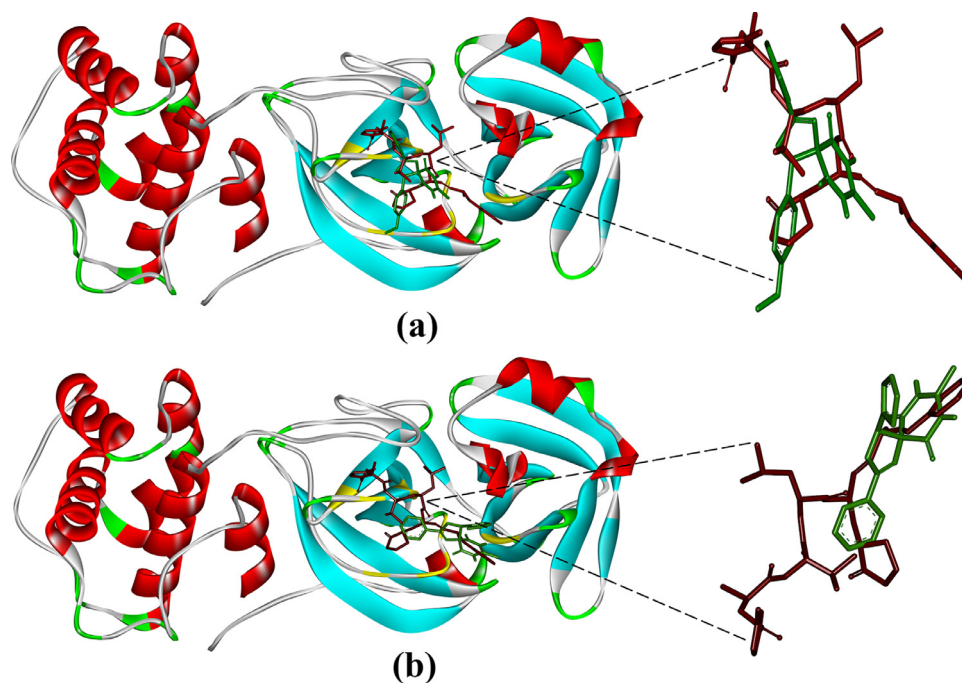
Fig. 9. The superposition of N3 (red) with spiroligands (green) DZ1 (a), and DZ2 (b) docked into the binding pocket of 7BQY residues.

DZ2 in the crystalline state significantly contribute to the ligand-protein interaction. The binding modes and various interaction types of DZ1 and DZ2 with the 7BQY protein were examined and shown in Fig. 8, respectively. Docking results revealed that ligand DZ1 showed good binding affinity towards protein with a −6.7 kcal/mol binding score. It has been documented that the GLY143 and GLU126 amino acid residue in Mpro are attractive sites for the formation of strong bonding interactions [56]. In the binding interactions of the DZ1 ligand, there are two conventional hydrogen bonds with ASN142 and other significant interactions with LEU141, GLU166, HIS164, GLN189 and THR190 are also observed (Table S6). Whereas in the binding interactions of DZ2 with 7BQY, three conventional hydrogen bonds were observed with THR26 and GLY143 (binding score = −6.7 kcal/mol). Further, three significant interactions with the potential amino acid candidates MET49 and CYS145 are also observed. A superposition diagram of the active sites of the 7BQY-N3 compound with the docked 7BQY-DZ1 and DZ2 compound were also drawn for the best comparison of the docked spirocompounds in the active site of 7BQY (Fig. 9). The 2D diagram of nonbonded interactions between the ligand (N3, DZ1 and DZ2) and the amino acid residues are represented in the supplementary Fig. S9. Finally, the molecular docking analysis reveals the major contribution of the N, O and S atoms of ligand in the effective interactions with the biomolecule. This could be attributed to the presence of lone-pair electrons on these atoms. Further, σ-π, anion-π and stacked-π contacts are the major contributors in hydrophobic interactions.

4. Conclusion

In the present study, we have systematically explored the conformational features of thioxotriaza-spirocrystal structures and the role of various non-covalent interactions in crystal packing. The single crystal structure analysis of DZ2 revealed that the fused carbon atom is in the rigid tetrahedral center, which connects the two perpendicular rings, and puckering analysis shows the envelope conformation on Cg(5) ring. The analysis of supramolecular self-assembly of the molecular structure shows that hydrogen bonding interactions are involved majorly in the crystal packing. We quantified the relative contribution and probability of various hydrogen bonding interactions (H…H, H…O, H…S and H…C) by the Hirshfeld surface and enrichment ratio analysis. The intermolecular interaction analysis of molecular structure shows four significant inversion dimers in DZ1 and three molecular pairs in DZ2 crystal structure. The energetics of interaction topologies for the hydrogen bonded molecular (dimer) pairs emphasized that the N-H…S contacts formed energetically least dimer with a larger contribution of electrostatic energy framework. While the cyclic pair of molecules with C–H…O interactions show the highest interaction energy with the dominant dispersion energy component. In conclusion, the designed spirobased derivatives have been investigated as an inhibitor for COVID-19 by an in-silico molecular docking study. Both DZ1 and DZ2 showed good binding affinity towards the main protease of COVID-19 with −6.7 kcal/mol. The result revealed that the spiroligands have a comparable binding affinity for SARSCoV-2 main protease to those of the approved medicines favipiravir and remdesivir, which have binding affinities −4.06 and −6.96 kcal/mol, respectively.

Declaration of Competing Interest

There are no conflicts of interest.

CRediT authorship contribution statement

Mahesha: Conceptualization, Formal analysis, Writing – original draft, Software. **Udaya Kumar A.H.:** Formal analysis, Writing – original draft, Software. **Vindya K.G.:** Data curation, Methodology. **Pampa K.J.:** Software, Validation, Data curation, Formal analysis, Investigation. **Rangappa K.S.:** Data curation, Methodology. **Lokanath N.K.:** Supervision, Conceptualization, Writing – review & editing.

Acknowledgements

Supplementary materials

Reference

[1] R.F. Keeler, Teratogenic compounds of veratrum californicum (durand) - VI: the structure of cyclopamine, Phytochemistry 8 (1969) 223–225, doi:10.1016/S0031-9422(00)85817-3.

[2] E.A. Jares-Erijman, A.L. Ingrum, J.R. Carney, K.L. Rinehart, R. Sakai, Polycyclic guanidine-containing compounds from the Mediterranean sponge crambe crambe: the structure of 13,14,15-Isocrambescidin 800 and the absolute stereochemistry of the pentacyclic guanidine moieties of the crambescidins, J. Org. Chem. 58 (1993) 4805–4808, doi:10.1021/JO00070A012.

[3] X. Wang, Z. Han, Z. Wang, K. Ding, Catalytic asymmetric synthesis of aromatic spiroketals by spinphox/iridium(I)-catalyzed hydrogenation and spiroketalization of α,α'-Bis(2-hydroxyarylidene) Ketones, angew. Chem. Int. Ed. 51 (2012) 936–940, doi:10.1002/ANIE.201106488.

[4] A.M. Kelley, E. Minerali, J.E. Wilent, N.J. Chambers, K.J. Stingley, G.T. Wilson, K.S. Petersen, Asymmetric synthesis of novel spirocycles via a chiral phosphoric acid catalyzed desymmetrization, Tetrahedron Lett. 60 (2019) 1262–1264, doi:10.1016/j.tetlet.2019.03.074.

[5] R.K.M. Khan, A.R. Zhugralin, S. Torker, R.V. O'Brien, P.J. Lombardi, A.H. Hoveyda, Synthesis, isolation, characterization, and reactivity of high-energy stereogenic-at-Ru carbenes: stereochemical inversion through olefin metathesis and other pathways, J. Am. Chem. Soc. 134 (2012) 12438–12441, doi:10.1021/JA3056722.

[6] A.K. Franz, N.V. Hanhan, N.R. Ball-Jones, Asymmetric catalysis for the synthesis of spirocyclic compounds, ACS Catal. 3 (2013) 540–553, doi:10.1021/CS300801Y.

[7] A. Baeyer, Systematik und nomenclatur bicyclischer kohlenwasserstoffe, Ber. Dtsch. Chem. Ges. 33 (1900) 3771–3775, doi:10.1002/CBER.190003303187.

[8] Y. Zheng, C.M. Tice, S.B. Singh, The use of spirocyclic scaffolds in drug discovery, Bioorg. Med. Chem. Lett. 24 (2014) 3673–3682, doi:10.1016/J.BMCL.2014.06.081.

[9] R. Pradhan, M. Patra, A.K. Behera, B.K. Mishra, R.K. Behera, Tetrahedron report number 747, Tetrahedron. 5 (2006) 779–828, doi:10.1016/J.TET.2005.09.039.

[10] J.Q. Zhang, Y. Gao, J. Song, D. Hu, M. Miao, H. Ren, Synthesis of spiro-cyclopropane oxindoles via michael-initiated cyclopropanation of pyridinium salts with 3-ylidene oxindoles, Synlett 32 (2021) 626–630, doi:10.1055/A-1327-6388.

[11] B. Zou, W.L. Chan, M. Ding, S.Y. Leong, S. Nilar, P.G. Seah, W. Liu, R. Karuna, F. Blasco, A. Yip, A. Chao, A. Susila, H. Dong, Q.Y. Wang, H.Y. Xu, K. Chan, K.F. Wan, F. Gu, T.T. Diagana, T. Wagner, I. Dix, P.-Y. Shi, P.W. Smith, Lead optimization of spiropyrazolopyridones: a new and potent class of dengue virus inhibitors, ACS Med. Chem. Lett. 6 (2015) 344–348, doi:10.1021/ML500521R.

[12] J. Xu, X. Xie, H. Chen, J. Zou, Y. Xue, N. Ye, P.Y. Shi, J. Zhou, Design, synthesis and biological evaluation of spiropyrazolopyridone derivatives as potent dengue virus inhibitors, Bioorg. Med. Chem. Lett. 30 (2020) 127162, doi:10.1016/J.BMCL.2020.127162.

[13] P. Zhou, X.L. Yang, X.G. Wang, B. Hu, L. Zhang, W. Zhang, H.R. Si, Y. Zhu, B. Li, C.L. Huang, H.D. Chen, J. Chen, Y. Luo, H. Guo, R.D. Jiang, M.Q. Liu, Y. Chen, X.R. Shen, X. Wang, X.S. Zheng, K. Zhao, Q.J. Chen, F. Deng, L.L. Liu, B. Yan, F.X. Zhan, Y.Y. Wang, G.F. Xiao, Z.L. Shi, A pneumonia outbreak associated with a new coronavirus of probable bat origin, Nature 579 (2012) 270–273, doi:10.1038/s41586-020-2012-7.

[14] D. Kuldeep, S. Khan, T. Ruchi, D. Maryam, M. Yashpal singh, S. Karam pal, C.W Chaicumpa, COVID-19, an emerging coronavirus infection: advances and prospects in designing and developing vaccines, immunotherapeutics, and therapeutics, Hum. Vaccin. Immunother. 16 (2020) 1232–1238, doi:10.1080/21645515.2020.1735227.

[15] T. Singhal, A review of coronavirus disease-2019 (COVID-19), Indian J. Pediatr. 87 (2020) 281–286, doi:10.1007/S12098-020-03263-6.

[16] D. Kumar, V. Chandel, S. Raj, B. Rathi, In silico identification of potent FDA approved drugs against coronavirus COVID-19 main protease: a drug repurposing approach, Chem. Biol. Lett. 7 (2020) 166–175 http://pubs.iscience.in/journal/index.php/cbl/article/view/1033. (accessed October 3, 2021).

[17] S. Bhatia, S. Giri, A.F. Lal, S. Singh, Identification of potential inhibitors of dietary polyphenols for SARS-CoV-2 M protease: an in silico study, Trop. Med. Health. 1 (2020) 21–29.

[18] G.R. Desiraju, Crystal engineering: from molecule to crystal, J. Am. Chem. Soc. 135 (2013) 9952–9967, doi:10.1021/JA403264C.

[19] S.K. Seth, I. Saha, C. Estarellas, A. Frontera, T. Kar, S. Mukhopadhyay, Supramolecular self-assembly of M-IDA complexes involving lone-pair···π interactions: crystal structures, Hirshfeld surface analysis, and DFT calculations [H2IDA = iminodiacetic acid, M = Cu(II), Ni(II)], Cryst. Growth Des. 11 (2011) 3250–3265, doi:10.1021/CG200506Q.

[20] K.L. Jyothi, Mahesha, N.K. Lokanath, Understanding the formation of novel hydrated gallic acid-creatinine molecular salt: crystal structure, Hirshfeld surface and DFT studies, J. Chem. Crystallogr. 50 (1234) (2021) 410–421, doi:10.1007/s10870-019-00814-4.

[21] V. Chandrasekhar, V. Krishnan, G.T.S. Andavan, A. Steiner, S. Zacchini, Cyclophosphazene supramolecular assemblies: N–H···N and C–H···N mediated supramolecular networks in the crystal structures of N3P3[N(Me)NH2]6 and spiro-N3P3[O2C12H8][N(Me)NH2]4, CrystEngComm 5 (2003) 245–247, doi:10.1039/B305694E.

[22] A.A. El-Emam, E.S. Kumar, K. Janani, L.H. Al-Wahaibi, O. Blacque, M.I. El-Awady, N.H. Al-Shaalan, M.J Percino, S. Thamotharan, Quantitative assessment of the nature of noncovalent interactions in N -substituted-5-(adamantan-1-yl)-1,3,4-thiadiazole-2-amines: insights from crystallographic and QTAIM analysis, RSC Adv. 10 (2020) 9840–9853, doi:10.1039/D0RA00733A.

[23] R. Shukla, P. Bandopadhyay, M. Sathe, D. Chopra, Quantitative investigation on the intermolecular interactions present in 8-(4-ethoxyphenyl)-1,3-dimethyl-3,7-dihydro-1H-purine-2,6-dione with insight from interaction energies, energy framework, electrostatic potential map and fingerprint analysis, J. Chem. Sci. 132 (2020) 1–7, doi:10.1007/S12039-019-1726-2.

[24] G.R. Desiraju, Crystal engineering: a brief overview, J. Chem. Sci. 122 (2010) 667–675, doi:10.1007/s12039-010-0055-2.

[25] T. Keškić, B. Čobeljić, M. Gruden, K. Andelković, A. Pevec, I. Turel, D. Radanović, M. Zlatar, What is the nature of interactions of BF4-, NO3-, and ClO4- to Cu(II) complexes with Girard's T hydrazine? When can binuclear complexes be formed? Cryst. Growth Des. 19 (2019) 4810–4821, doi:10.1021/ACS.CGD.9B00760.

[26] V.K. Gopinatha, H.A. Swarup, S.C. Raghavan, K. Mantelingu, K.S. Rangappa, Discovery of novel approach for regioselective synthesis of thioxotriaza-spiro derivatives via oxalic acid, Synlett 30 (2019) 2004–2009, doi:10.1055/S-0039-1690204.

[27] C.C.S. Rigaku, Expert 2.0 r15, Rigaku Corporation, Tokyo, Japan, 2011.

[28] G.M. Sheldrick, A short history of SHELX, Acta Crystallogr. Sect. A Found. Crystallogr. 64 (2008) 112–122, doi:10.1107/S0108767307043930.

[29] G.M. Sheldrick, Crystal structure refinement with SHELXL, Acta. Cryst-C. 71 (2015) 3–8, doi:10.1107/S2053229614024218.

[30] O.V. Dolomanov, L.J. Bourhis, R.J. Gildea, J.A.K. Howard, H. Puschmann, OLEX2: a complete structure solution, refinement and analysis program, J. Appl. Crystallogr. 42 (2009) 339–341, doi:10.1107/S0021889808042726.

[31] A.L. Spek, Structure validation in chemical crystallography, Acta Crystallogr. Sect. D Biol. Crystallogr. 65 (2009) 148–155, doi:10.1107/S090744490804362X.

[32] C.F. Macrae, I. Sovago, S.J. Cottrell, P.T.A. Galek, P. McCabe, E. Pidcock, M. Platings, G.P. Shields, J.S. Stevens, M. Towler, P.A. Wood, IUCr, mercury 4.0: from visualization to analysis, design and prediction, J. Appl. Crystallogr. 53 (2020) 226–235, doi:10.1107/S1600576719014092.

[33] M.A. Spackman, D. Jayatilaka, Hirshfeld surface analysis, CrystEngComm 11 (2009) 19–32, doi:10.1039/B818330A.

[34] J.J. McKinnon, M.A. Spackman, A.S. Mitchell, IUCr, novel tools for visualizing and exploring intermol-ecular interactions in molecular crystals, Acta Crystallogr., Sect. B: Struct. Sci. 60 (2004) 627–668, doi:10.1107/S0108768104020300.

[35] M.A. Spackman, J.J. McKinnon, Fingerprinting intermolecular interactions in molecular crystals, CrystEngComm 4 (2002) 378–392, doi:10.1039/b203191b.

[36] C. Jelsch, K. Ejsmont, L. Huder, The enrichment ratio of atomic contacts in crystals, an indicator derived from the Hirshfeld surface analysis, IUCrJ 1 (2014) 119–128, doi:10.1107/S2052252514003327.

[37] M.W. Shi, S.P. Thomas, G.A. Koutsantonis, M.A. Spackman, Supramolecular recognition and energy frameworks in host–guest complexes of 18-crown-6 and sulfonamides, Cryst. Growth Des. 15 (2015) 5892–5900, doi:10.1021/ACS.CGD.5B01316.

[38] C.F. Mackenzie, P.R. Spackman, D. Jayatilaka, M.A. Spackman, CrystalExplorer model energies and energy frameworks: extension to metal coordination compounds, organic salts, solvates and open-shell systems, IUCrJ 4 (2017) 575–587, doi:10.1107/S2052252514003327.

[39] M.J. Frisch, G.W. Trucks, H.B. Schlegel, G.E. Scuseria, M.A. Robb, J.R. Cheeseman, G. Scalmani, V. Barone, G.A. Petersson, H. Nakatsuji, X. Li, M. Caricato, A.V. Marenich, J. Bloino, B.G. Janesko, R. Gomperts, B. Mennucci, H.P. Hratchian, J.V. Ortiz, A.F. Izmaylov, J.L. Sonnenberg, D. Williams-Young, F. Ding, F. Lipparini, F. Egidi, J. Goings, B. Peng, A. Petrone, T. Henderson, D. Ranasinghe, V.G. Zakrzewski, J. Gao, N. Rega, G. Zheng, W. Liang, M. Hada, M. Ehara, K. Toyota, R. Fukuda, J. Hasegawa, M. Ishida, T. Nakajima, Y. Honda, O. Kitao, H. Nakai, T. Vreven, K. Throssell, J.A. Montgomery Jr., J.E. Peralta, F. Ogliaro, M.J. Bearpark, J.J. Heyd, E.N. Brothers, K.N. Kudin, V.N. Staroverov, T.A. Keith, R. Kobayashi, J. Normand, K. Raghavachari, A.P. Rendell, J.C. Burant, S.S. Iyengar, J. Tomasi, M. Cossi, J.M. Millam, M. Klene, C. Adamo, R. Cammi, J.W. Ochterski, R.L. Martin, K. Morokuma, O. Farkas, J.B. Foresman, D.J. Fox, Gaussian 16, Revision C.01, Gaussian, Inc., Wallingford CT, 2016.

[40] Dennington R. D., Keith T. A., and Millam J. M., Semichem Inc., Shawnee Mission, KS, (2016) GaussView 6.0.16.

[41] N.K. Nkungli, J.N. Ghogomu, Theoretical analysis of the binding of iron(III) protoporphyrin IX to 4-methoxyacetophenone thiosemicarbazone via DFT-D3, MEP, QTAIM, NCI, ELF, and LOL studies, J. Mol. Model. 23 (2017) 1–20, doi:10.1007/S00894-017-3370-4.

[42] T. Lu, F. Chen, Multiwfn: a multifunctional wavefunction analyzer, J. Comput. Chem. 33 (2012) 580–592, doi:10.1002/JCC.22885.

[43] W. Humphrey, A. Dalke, K. Schulten, VMD: visual molecular dynamics, J. Mol. Graph. 14 (1996) 33–38, doi:10.1016/0263-7855(96)00018-5.

[44] E. Di Muzio, D. Toti, F. Polticelli, DockingApp: a user friendly interface for facilitated docking simulations with autodock vina keywords molecular docking · virtual screening · drug repurposing · graphic interface · wrapper · autodock vina, J. Comput. Aided. Mol. Des. 31 (2017) 213–218, doi:10.1007/s10822-016-0006-1.

[45] Dassault Systèmes D.S. Biovia, Discovery Studio Modeling Environment, (2017). Dassault Systèmes, San Diego., CA, USA:2017.

[46] Z. Jin, X. Du, Y. Xu, Y. Deng, M. Liu, Y. Zhao, B. Zhang, X. Li, L. Zhang, C. Peng, Y. Duan, J. Yu, L. Wang, K. Yang, F. Liu, R. Jiang, X. Yang, T. You, X. Liu, X. Yang, F. Bai, H. Liu, X. Liu, L.W. Guddat, W. Xu, G. Xiao, C. Qin, Z. Shi, H. Jiang, Z. Rao, H. Yang, Structure of Mpro from SARS-CoV-2 and discovery of its inhibitors, Nature 582 (2020) 289–293 2020 5827811, doi:10.1038/s41586-020-2223-y.

[47] D.G. Evans, J.C.A. Boeyens, IUCr, Conformational analysis of ring pucker, Acta Cryst. (1989). B 45 (1989) 581–590, doi:10.1107/S0108768189008190.

[48] M.K.H Mahesha, C.S. Karthik, K.J. Pampa, P. Mallu, N.K. Lokanath, Solvent induced mononuclear and dinuclear mixed ligand Cu(II) complex: structural diversity, supramolecular packing polymorphism and molecular docking studies, New J. Chem. 44 (2020) 18048–18068, doi:10.1039/D0NJ03567J.

[49] A.H.U. Kumar, K. Kumara, N.V. Harohally, K.J. Pampa, N.K. Lokanath, Square planar trans-N_2O_2 Cu(II) Complex: synthesis, crystal structure, Hirshfeld surface, DFT, antimicrobial and docking studies, ChemistrySelect 6 (2021) 6240–6255, doi:10.1002/SLCT.202101149.

[50] M.A. Alsafi, D.L. Hughes, M.A. Said, First COVID-19 molecular docking with a chalcone-based compound: synthesis, single-crystal structure and Hirshfeld surface analysis study, Acta. Cryst-C 76 (2020) 1043–1050, doi:10.1107/S2053229620014217.

[51] D. Dey, S. Bhandary, S.P. Thomas, M.A. Spackman, Deepak Chopra, Energy frameworks and a topological analysis of the supramolecular features in in situ cryocrystallized liquids: tuning the weak interaction landscape via fluorination, Phys. Chem. Chem. Phys. 18 (2016) 31811–31820, doi:10.1039/C6CP05917A.

[52] D.A. Safin, C.M.L. Vande Velde, M.G. Babashkina, K. Robeyns, Y. Filinchuk, Mononuclear heteroleptic complexes of copper(I) with 5-phenyl-2,2′-bipyridine and triphenylphosphine: crystal structures, Hirshfeld surface analysis and luminescence properties, New J. Chem. 40 (2016) 6156–6163, doi:10.1039/C6NJ00833J.

[53] K.J.P Mahesha, C.S. Karthik, M.K. Hema, P. Mallu, N.K. Lokanath, Post-synthetic modification of supramolecular assemblies of β-diketonato Cu(II) complexes: comparing and contrasting the molecular topology by crystal structure and quantum computational studies, CrystEngComm 23 (2021) 4344–4369, doi:10.1039/D1CE00304F.

[54] E. Espinosa, E. Molins, C. Lecomte, Hydrogen bond strengths revealed by topological analyzes of experimentally observed electron densities, Chem. Phys. Lett. 285 (1998) 170–173, doi:10.1016/S0009-2614(98)00036-0.

[55] T.C.R Mahesha, M.K. Hema, K.J. Pampa, P.G. Chandrashekara, K. Mantelingu, T. Demappa, N.K. Lokanath, Analysis of supramolecular self-assembly of two chromene derivatives: synthesis, crystal structure, Hirshfeld surface, quantum computational and molecular docking studies, J. Mol. Struct. 1225 (2021) 129104, doi:10.1016/J.MOLSTRUC.2020.129104.

[56] B. Shah, P. Modi, S.R. Sagar, In silico studies on therapeutic agents for COVID-19: drug repurposing approach, Life Sci 252 (2020) 117652, doi:10.1016/J.LFS.2020.117652.